



Atomization driven crystalline nanocarbon based single-atom catalysts for superior oxygen electroreduction

Jae Young Jung^{a,b}, Haneul Jin^c, Min Woo Kim^{a,b}, Sungjun Kim^{d,e}, Jeong-Gil Kim^a, Pil Kim^f, Yung-Eun Sung^{d,e}, Sung Jong Yoo^{g,h,i,*}, Nam Dong Kim^{a,**}

^a Functional Composite Materials Research Center, Korea Institute of Science and Technology (KIST), Jeollabuk-do 55324, Republic of Korea

^b Department of Materials Science & Engineering, Gwangju Institute of Science & Technology (GIST), Gwangju 61005, Republic of Korea

^c Department of Energy and Materials Engineering, Dongguk University-Seoul, Seoul 04620, Republic of Korea

^d Center for nanoparticle research, Institute for Basic Science (IBS), Seoul 08826, Republic of Korea

^e School of Chemical and Biological Engineering, Seoul National University (SNU), Seoul 08826, Republic of Korea

^f School of Chemical Engineering, School of Semiconductor and Chemical Engineering, Clean Energy Research Center, Jeonbuk National University, Jeonju 54896, Republic of Korea

^g Hydrogen-Fuel Cell Research Center, Korea Institute of Science and Technology (KIST), Seoul 02792, Republic of Korea

^h KHU-KIST Department of Converging Science and Technology, Kyung Hee University, 26, Kyungheedaero-ro, Dongdaemun-gu, Seoul 02447, Republic of Korea

ⁱ Division of Energy & Environment Technology, KIST School, University of Science and Technology (UST), Daejeon 34113, Republic of Korea

ARTICLE INFO

Keywords:

Single atom catalysts
Atom-migration-trapping
M-N_x-C catalysts
Oxygen reduction reaction
Anion exchange membrane fuel cells

ABSTRACT

Atom-migration-trapping (AMT) is an effective and straightforward strategy for fabricating single-atom catalysts (SACs), but understanding the mechanism and effects of anchoring sites on AMT are formidable challenges. Here, we demonstrate that AMT phenomena occurs in crystalline porous nanocarbon, which allows development of highly efficient SACs via systematic investigation of atomization process and chemical state of active sites. An arc discharge-based bottom-up synthesis can generate an ideal porous nanocarbon with controllable nitrogen functionality, containing metal nanoparticles for AMT. Pre-formed N-functionalities in as-synthesized catalyst play important role in capturing single metal species, while additional ammonia treatment successfully modulates coordination geometry of active sites. The atomic cobalt catalyst exhibits superior oxygen reduction activity with remarkable power performance in single-cell experiments (752 mW cm^{-2}), exceeding the reported Co-N atomic catalysts. Our findings provide not only new perspectives in AMT phenomena but also strategies to develop an efficient and practical SACs in energy conversion systems.

1. Introduction

Single-atom catalysts (SACs) with unique electronic structures and coordination environments have recently emerged as a promising new class of catalytic materials [1–6]. Isolated single metal atoms were stabilized by chemical bonding to the support atoms, which can maximize atom utilization efficiency and provide remarkable catalytic properties such as extraordinary catalytic selectivity and activity in various catalytic reactions [7–11]. Recently, a variety of synthetic strategies for fabricating SACs have been reported. Wet-chemical approaches, including defect engineering and spatial confinement strategies, are widely applied using precursors under proper synthesis conditions. However, recent SAC synthesis methods generally have requirements for

either multistep synthesis and/or high-temperature annealing [4, 12–15]. Under these circumstances, single metal atoms readily tend to agglomerate into larger particles. The carbon supports obtained from recent methods have quite defective and amorphous characteristics. This leads to a decrease in and deactivation of catalytic reactivity, which is a major obstacle to the commercialization of SACs [16–19].

Specifically, an atom-migration-trapping (AMT) strategy involving the direct transformation from bulk to single metal atoms is an effective and straightforward route for fabricating high-loading single-atom catalysts (SACs) [20]. During the AMT process, bulk metals emit mobile metal atoms at a high temperature; these atoms can be stabilized on an appropriate support by creating stable chemical bonds with heteroatoms such as nitrogen, oxygen, and phosphorus [21–27]. Moreover, the single

* Corresponding author at: Hydrogen-Fuel Cell Research Center, Korea Institute of Science and Technology (KIST), Seoul 02792, Republic of Korea.

** Corresponding author.

E-mail addresses: ysj@kist.re.kr (S.J. Yoo), ndkim@kist.re.kr (N.D. Kim).

<https://doi.org/10.1016/j.apcatb.2022.122172>

Received 23 September 2022; Received in revised form 2 November 2022; Accepted 9 November 2022

Available online 17 November 2022

0926-3373/© 2022 The Authors. Published by Elsevier B.V. This is an open access article under the CC BY-NC-ND license (<http://creativecommons.org/licenses/by-nc-nd/4.0/>).

atom sites derived from the AMT process are thermally stable because synthetic parameters such as high temperature ensure that only thermally stable anchoring sites participate in stabilizing metal atoms during synthesis. Single metal atoms on nitrogen-doped carbons derived from metal-organic frameworks (MOFs) and nitrogen-containing polymeric layer deposition are representative examples using AMT phenomena [28–30]. The confinement of metal nanoparticles within the pores of MOFs and polymer networks is the first requirement for suppressing particle migration and sintering during atomization. As a second requirement, the nitrogen functional groups in pyrolysis-derived amorphous carbon are key elements for stabilizing the mobile metal atoms vaporized from nanoparticles and forming M-N bonds.

Despite the significant importance of nitrogen anchoring sites, understanding their effects on AMT is still difficult and unresolved because the reported synthetic approaches are simultaneously incorporate carbonization and atomization. In this synthetic environment, drastic structural collapse of the nanostructure occurs, and the nitrogen sites around metal particles change rapidly in the process of carbonization [28]. These limitations can be alleviated by using highly crystalline nanocarbon materials that are thermally and structurally stable at high AMT temperatures. However, to the best of our knowledge, these AMT processes have not been demonstrated in crystalline nanocarbon materials without using other nitrogen-containing support materials. This is because it has been very challenging to confine metal nanoparticles in porous crystalline nanocarbon structures. Additionally, it is desirable for the nitrogen anchoring sites of nanocarbons to be tunable to clearly investigate the effect of nitrogen sites on the AMT process. In this regard, our recently reported bottom-up synthesis strategy would provide great opportunities for the synthesis of highly crystalline porous nanocarbons with controllable nitrogen functionalities and the possibility for the direct incorporation of metal nanoparticles inside [31]. Thus, systematic investigation for both effects of nitrogen anchoring sites on atomic sites and atomization mechanism will help the development of highly efficient SACs for practical applications.

Herein, we demonstrate a new route to fabricate high loading single atomic sites on a hierarchical porous crystalline nanocarbon structure from AMT process as a high performance AEMFC catalyst. The role of nitrogen anchoring sites in the AMT process was systematically investigated. Metal nanoparticles were successfully introduced into porous nanocarbon structures with high crystallinity and abundant nitrogen functionality via bottom-up arc synthesis. The nitrogen site density could be controlled by changing the chamber pressure. It was confirmed that the number of nitrogen anchoring sites affected on the degree of atomization. Even in the absence of nitrogen anchoring sites, atomization was promoted by additional nitrogen doping through ammonia annealing. In situ Transmission Electron Microscope (TEM) and temperature-resolved X-ray absorption fine structure (XAFS) analysis were applied to reveal the detailed process and mechanism of AMT. The synthesized catalyst was applied to the oxygen reduction reaction (ORR), and the most active catalysts showed significantly enhanced ORR activity and good durability compared to those of commercial platinum catalysts. In a single-cell experiment, the synthesized catalyst showed a high power density of 752 mW cm^{-2} , which is much higher than that of the reported Co-N₄-C atomic catalysts.

2. Experimental

2.1. Materials

The graphitic carbon rod used as the anode electrode was purchased from DAEHAN CARBON Co., Ltd. The Vulcan XC-72 carbon powder was obtained from Cabot. Triple-distilled water was used. Isopropyl alcohol (IPA) and acetone were obtained from SAMCHUN CHEMICAL. Nafion perfluorinated resin in alcohol solution (5 wt%) and CoCl₂ hexahydrate were obtained from Sigma Aldrich. Commercial platinum catalysts (Pt/C, 20 wt%) were obtained from Alfa Aesar and used as a reference ORR

catalyst in this work.

2.2. Synthesis of Co_{NP}/CNH_{x%}

For the arc discharge synthesis of pristine Co_{NP}/CNH_{x%}, 0.6 g of CoCl₂ was dissolved in 150 mL acetone and sonicated with 0.6 g of Vulcan XC-72 for 10 min. To obtain CoCl₂/Vulcan XC-72 composites, a mixed solution was added to round flakes and dried by a rotary evaporator in a 45 °C water reservoir at 140 rpm. The obtained CoCl₂/Vulcan XC-72 mixed powder was annealed under a nitrogen atmosphere at 950 °C for 1 hr. Materials consisting of the graphitic carbon rod and CoCl₂/Vulcan XC-72 mixed powder were used as anode electrodes. A cylindrical graphite electrode was used as the cathode electrode. The direct current arc discharge (the applied voltage and current between the cathode and anode were 30 V and 150 A) was performed at a pressure of 50 Torr and 300 Torr under a N₂ atmosphere. After arc discharge synthesis, the chamber was cooled to room temperature under vacuum. The pristine Co_{NP}/CNH_{x%} catalysts were collected on the chamber wall. The obtained nanocarbon was denoted as Co_{NP}/CNH_{3.6%} for the 50 Torr condition and Co_{NP}/CNH_{8.1%} for the 300 Torr condition. The pristine Co_{NP}/CNH_{x%} catalysts were annealed under air at 350 °C with a 5 °C min⁻¹ ramping rate. Then, the air-annealed catalysts were directly annealed under a N₂ or NH₃ atmosphere at 700 °C with a 5 °C min⁻¹ ramping rate. The final catalysts were denoted as Co_{NP}/CNH_{3.6%} N₂ or NH₃ and Co_{NP}/CNH_{8.1%} N₂ or NH₃.

2.3. Characterization

The cobalt content of the overall catalysts was obtained with an ICPs instrument (inductively coupled plasma spectroscopy, ICPs-7500, Japan). The powder sample was stirred in HCl and HNO₃ mixed solution to remove every metal species. The X-ray diffraction (XRD) analysis was performed to investigate the crystalline properties of samples using 1D-Rigaku Smartlab 3. The nitrogen adsorption/desorption isotherms were measured to obtain the Brunauer-Emmett-Teller (BET) surface area and pore sized distribution in the range of micropore (Horvath-Kawazoe model, HK) and meso-macropore (Barrett-Joyner-Halenda, BJH) using 3FLEX equipment. The X-ray photoelectron spectroscopy (XPS) analysis was performed with a Thermo Fisher, USA, instrument equipped with a monochromatic Al K α ($h\nu = 1000 \text{ eV}$) (Multilab 2000). Transmission electron microscopy (TEM) was performed with a Tecnai G2 F20, USA, operated at an accelerating voltage of 200 kV. HAADF-STEM images were obtained with a TitanTM 80–300 operated at an accelerating voltage of 200 kV. In situ TEM analysis was conducted using “Fusion Select” in situ heating holders from Protochips Inc. at a ramping rate of 1 °C s⁻¹. The duration of observation was 5 min at 600, 700, 800, and 900 °C to investigate the AMT process. The X-ray absorption fine structure (XAFS) spectra of the catalysts were measured in an 8 C nanoprobe XAFS beamline at the Pohang Accelerator Laboratory Light Source (PLS-II), with a ring current of 360 mA in a 3.0 GeV storage ring. A Si(111) double crystal monochromated the X-ray beam. The intensity of the synchrotron beam was reduced by 30 % to eliminate the higher-order harmonics. The XAFS spectra were collected by transmission modes. The measured XAFS data were processed and analyzed using the software Demeter. The EXAFS curves were fitted using software Artemis in the k-space range of 3–11 Å⁻¹ with a Hanning window. For the in situ XAFS measurements, 60 mg of Co_{NP}/CNH_{8.1%} sample was pelletized using a press equipment, and the pellet thickness was 2 mm. The temperature programmed in situ XAFS spectra were collected by transmission modes. The temperature was varied from room temperature (RT) to 700 °C with a 20 °C min⁻¹ ramping rate, using a N₂ gas flow cell. The duration of EXAFS measurements was kept for 30 min at RT, 100, 200, 500, 600 and 700 °C.

2.4. Electrochemical characterization

The overall electrochemical measurements were conducted by a potentiostat (CHI 920 C) with a glassy carbon electrode (area = 0.2472 cm²) as the working electrode, Pt wire as the counter electrode, and Hg/HgO as the reference electrode (1 M NaOH) with an electrode rotating system. The catalyst ink was prepared by mixing and sonicating 2 mg of catalyst, 10 μ l of Nafion solution, and 100 μ l of DI water and IPA for 30 min. Specific amounts of ink were dropped onto a glassy carbon electrode to achieve a catalyst loading of 400 μ g_{cat} cm⁻²_{geo}. For reference catalysts, 12 μ g_{pt} cm⁻²_{geo} of commercial Pt/C (20 wt%, Alfa Aesar) was loaded onto a glassy carbon disk electrode. Linear sweep voltammetry (LSV) was conducted in oxygen-saturated 0.1 M KOH electrolyte in the potential range between 0.100 and 1.100 V_{RHE} with a potential scan rate of 10 mV s⁻¹. The disk rotating speed was set at 1600 rpm. To obtain HO₂⁻ fraction and electron transfer number (n), rotating ring-disk electrode (RRDE) experiments were conducted at a ring potential of 1.3 V vs. RHE. The fraction of HO₂⁻ and n was calculated using the following equations [32].

$$n = \frac{4}{1 + \frac{i_R}{N \cdot i_D}} \quad (1)$$

$$\text{The fraction of } HO_2^- = 2 \times \frac{\frac{i_R}{N}}{i_D + \frac{i_R}{N}} \quad (2)$$

In the equations, i_R and i_D are the measured currents for ring electrode and disk electrode. N is the conversion efficiency factor of the ring electrode (0.44). The chronoamperometry experiments were conducted at a potential of 0.8 V vs. RHE for 50,000 s in the oxygen-saturated 0.1 M KOH. Accelerated potential cycling tests were performed by cycling in the potential range from 0.6 to 1.0 V_{RHE} at a scan rate of 100 mV s⁻¹ under oxygen-saturated 0.1 M KOH electrolyte for 15,000 cycles. To calibrate the electrode potential, the thermodynamic potential for RHE was the potential when the disk current was zero in 0.1 M KOH with a platinum wire (working electrode) under H₂ saturation.

2.5. Fuel cell tests

Membrane electrode assemblies (MEAs) were fabricated by catalyst-coated membranes (CCM) through hand spraying. The membrane was

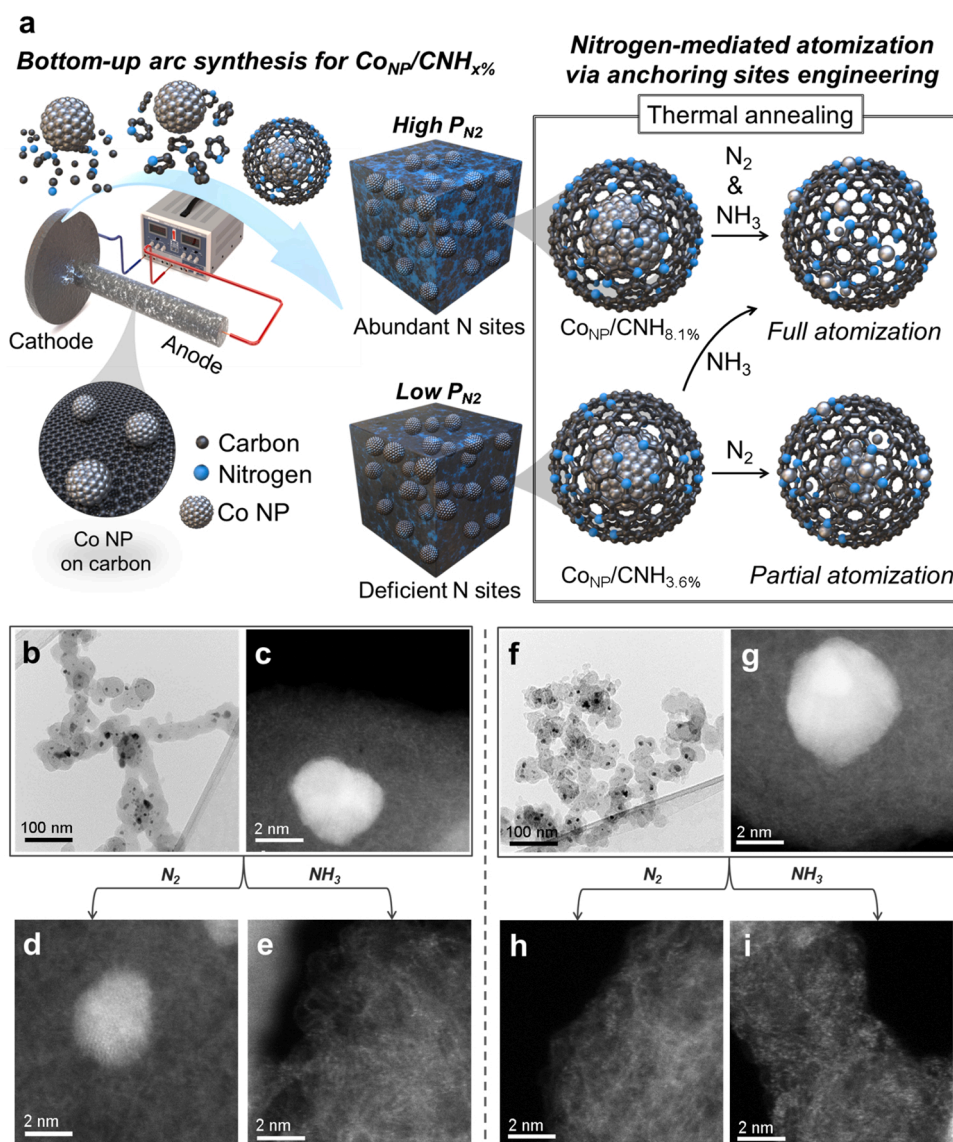


Fig. 1. (a) Schematic illustration of research. (b) TEM images of Co_{NP}/CNH_{3.6%}. (c-e) HAADF-STEM images of Co_{NP}/CNH_{3.6%}, Co_{NP}/CNH_{3.6%} N₂, and Co_{NP}/CNH_{3.6%} NH₃. (f) TEM images of Co_{NP}/CNH_{8.1%}. (g-i) HAADF-STEM images of Co_{NP}/CNH_{8.1%}, Co_{NP}/CNH_{8.1%} N₂, and Co_{NP}/CNH_{8.1%} NH₃.

FAA-3-50. The catalyst was mixed with I2 ionomer (Acta S.P. A), IPA (99.99 %, Burdick & Jackson) and DI water under stirring and ultrasonication. The ionomer/catalyst mass ratio was set at 0.5. For anode fabrication, commercial PtRu/C (60 wt%, Johnson Matthey) was used with a Pt loading of 0.4 mg cm^{-2} . The cathode was $\text{Co}_{\text{NP}}/\text{CNH}_{x\%} \text{ NH}_3$ with a catalyst loading of 1.0 mg cm^{-2} . The prepared MEAs were treated with 1 M NaOH solution for 24 h and then washed with DI water. The MEA size was 5 cm^2 , and it was sandwiched between gas diffusion layers (GDLs) to form a single-cell device. We used JNTG-30-A6H and JNT-30-A6H as anode/cathode diffusion media. The selected flow field plates were serpentine type with a single flow channel (area of 1 mm^2). Single cells were applied with a fully humidified gas flow for both H_2 (0.8 L min^{-1} , relative humidity $\sim 85 \%$) and O_2 (1.0 L min^{-1} , relative humidity $\sim 95 \%$) at 60°C .

3. Results and discussion

3.1. Synthesis and morphology analysis of $\text{Co}_{\text{NP}}/\text{CNH}_{x\%}$ with different thermal annealing

Fig. 1a illustrates the proposed AMT process from cobalt nanoparticle (Co-NP) to single cobalt atom with a controlled density of nitrogen anchoring site in crystalline nano-carbon structures. A Vulcan XC-72 and CoCl_2 were dissolved in acetone and stirred for homogeneous deposition of Co ions on the surface of Vulcan XC-72, as previously reported [31]. The obtained precursor powder of Co/Vulcan XC-72 mixture were closely packed in a graphite rod and then annealed at 950°C for further increase of electric conductivity of filler materials. During this process, Co species present on the surface of Vulcan XC-72 are spontaneously aggregated to form numerous amounts of Co-NPs. In the subsequent arc-discharge process, highly crystalline N-doped nanocarbons was synthesized from the reassemble of ionized C and N species in the arc plasma. The amount of N functionalities could be simply controlled by adjusting the chamber pressure filled with N_2 gas. On the other hand, Co-NPs could not be fully ionized during the short reaction time of arc plasma, and directly incorporated in the porous structure of N-doped nanocarbon. It should be emphasized that the presence of Co-NPs in the porous network of N-doped nanocarbon, which was possible due to the bottom-up arc discharge synthesis method, is critical for the efficient AMT process, because numerous N-doping sites surrounding the Co-NPs play an important role in capturing the emitted Co atoms from the NPs.[28] Co-NPs were found almost everywhere in the as-synthesized sample regardless of nitrogen functionality (Fig. 1b-d and Fig. S1). The morphology and size of these Co-NPs are quite uniform in the range of 3–10 nm. Two types of samples with different amounts of N-doping contents were chosen as representative models for this study. The nitrogen content of the catalyst was found to be 3.6 at% and 8.1 at% under pressures of 50 Torr and 300 Torr, respectively and these catalysts are denoted as $\text{Co}_{\text{NP}}/\text{CNH}_{3.6\%}$ and $\text{Co}_{\text{NP}}/\text{CNH}_{8.1\%}$, respectively (Table S1). The amounts of cobalt species are confirmed by ICP analysis and found to be quite similar as 0.226 at% and 0.234 at% for $\text{Co}_{\text{NP}}/\text{CNH}_{3.6\%}$ and $\text{Co}_{\text{NP}}/\text{CNH}_{8.1\%}$, respectively, indicating that metal content was not affected by the chamber pressure of N_2 gas.

To investigate the role of nitrogen functionality on the AMT process, both samples were post-annealed under different atmosphere of N_2 and NH_3 . As shown in Fig. S2, the pristine $\text{Co}_{\text{NP}}/\text{CNH}_{x\%}$ catalysts exhibited only carbon nanohorn features without metal-related diffraction peaks, possibly indicating that the small amounts of cobalt nanoparticles are undetectable by XRD. There are no any significant changes in the crystalline structure of nanohorns even after the post-annealing processes, indicating the excellent thermal stability of carbon structure. Interestingly, the sharp diffraction features marked as green stars becomes more distinct after thermal treatment, indicating the removal of thermally unstable carbonaceous species such as amorphous carbons. As shown in Fig. S3, the BET surface area of pristine $\text{Co}_{\text{NP}}/\text{CNH}_{8.1\%}$ ($156.36 \text{ m}^2 \text{ g}^{-1}$)

dramatically increased to $538.18 \text{ m}^2 \text{ g}^{-1}$ for $\text{Co}_{\text{NP}}/\text{CNH}_{8.1\%} \text{ N}_2$ and $649.45 \text{ m}^2 \text{ g}^{-1}$ for $\text{Co}_{\text{NP}}/\text{CNH}_{8.1\%} \text{ NH}_3$, which is attributed to the development of hierarchical pore structure within the carbon nanohorns. It is considered that annealing in N_2 condition provide only thermal activation effect, while annealing in NH_3 condition provide additional nitrogen doping effect. Therefore, the effect of pre-existing N functionalities on AMT process can be elucidated by analyzing the samples after annealing in N_2 atmosphere ($\text{Co}_{\text{NP}}/\text{CNH}_{3.6\%} \text{ N}_2$ and $\text{Co}_{\text{NP}}/\text{CNH}_{8.1\%} \text{ N}_2$). In the case of $\text{Co}_{\text{NP}}/\text{CNH}_{3.6\%} \text{ N}_2$, some of the large Co-NPs still remain inside the carbon structure after thermal annealing process which indicates atomization does not proceed completely at deficient densities of nitrogen functionalities (Fig. 1d and Fig. S4a). It should be emphasized that some cobalt atoms are observed (Fig. S4b). It is assumed that the thermally emitted cobalt atoms are partially atomized and that the rest of the cobalt species are agglomerated due to the insufficient capacity to capture metal atoms on nitrogen sites. On the other hands, any particular types of Co species cannot be found in $\text{Co}_{\text{NP}}/\text{CNH}_{8.1\%} \text{ N}_2$ and individual Co atoms can be confirmed from the TEM and HAADF-STEM analysis (Fig. 1h, Fig. S4c). This demonstrated that the density of nitrogen sites around metal particles affects the degree of atomization. As shown in the results of our previous studies, ammonia annealing can introduce additional nitrogen sites on a carbon lattice [33, 34]; ammonia annealing was performed at the same temperature for comparison. We expect additional nitrogen sites to affect the atomization process. Unlike $\text{Co}_{\text{NP}}/\text{CNH}_{3.6\%} \text{ N}_2$, there are no Co-NPs in $\text{Co}_{\text{NP}}/\text{CNH}_{3.6\%} \text{ NH}_3$, and single Co atoms embedded in carbon are observed (Fig. S5a and Fig. 1e). The Co-NPs disappear in $\text{Co}_{\text{NP}}/\text{CNH}_{8.1\%} \text{ NH}_3$ (Fig. 1i and Fig. S5b). It is noteworthy that ammonia facilitates AMT even at deficient anchoring site densities, suggesting that ammonia acts as a promoter by modulating nitrogen functional groups. The ICP analysis showed that the cobalt contents increase after thermal annealing due to the removal of thermally unstable amorphous carbon (Table S1). The disappearance of Co-NPs is mainly due to atomization rather than vaporization. The cobalt loadings in the $\text{Co}_{\text{NP}}/\text{CNH}_{3.6\%} \text{ NH}_3$ and $\text{Co}_{\text{NP}}/\text{CNH}_{8.1\%} \text{ NH}_3$ reached to 0.420 at% (2.03 wt%) and 0.456 at% (2.20 wt%) respectively, achieving 1.75 and 1.90 times higher Co loading than that of previous Co-SACs using arc discharge methods [31]. This indicated that the outstanding ability of the Co-NPs confinement strategy within the pores of highly crystalline nanocarbon using bottom-up arc synthesis, suppressing the formation of Co-NPs or clusters during high-temperature AMT process.

3.2. The critical roles of nitrogen anchoring sites in stabilizing metal atoms during atomization

X-ray photoelectron spectroscopy (XPS) was performed to investigate the properties of the nitrogen functional groups. As shown in Fig. 2a, the high-resolution N 1s XPS spectra can be divided into three types of nitrogen functional groups: pyridinic N (N-6) ($398.6 \pm 0.2 \text{ eV}$), pyrrolic N (N-5) ($400.2 \pm 0.2 \text{ eV}$), and quaternary N (N-Q) ($401.5 \pm 0.2 \text{ eV}$). The atomic contents of each N state are shown in Fig. 2b and Table S1. The initial composition of the nitrogen functional groups in $\text{Co}_{\text{NP}}/\text{CNH}_{3.6\%}$ is 74.25% for N-6, 21.42% for N-5, and 4.33 % for N-Q, which is very similar to that of $\text{Co}_{\text{NP}}/\text{CNH}_{8.1\%}$ even with different amounts of nitrogen doping. It has been well known that the nitrogen functional groups serve anchoring sites for metal atoms; especially, the structure of N-6 and N-5 play important roles for fabricating atomic M-N_x-C sites during thermal driven atomization [28]. A close investigation on the nature of nitrogen functionalities in each steps of catalyst fabrication can provide valuable insight of their role for the atomization. Total amount of nitrogen functional group has been slightly decreased after the air and successive N_2 post-annealing process (2.40 at% for $\text{Co}_{\text{NP}}/\text{CNH}_{3.6\%} \text{ N}_2$ and 6.20 at% for $\text{Co}_{\text{NP}}/\text{CNH}_{8.1\%} \text{ N}_2$) (Fig. 2b). This is probably because of the removal of amorphous carbon impurities on the surface of CNH structure and pore opening process starting from the defective part of CNH, i.e. N-doping sites, resulting in a loss of some

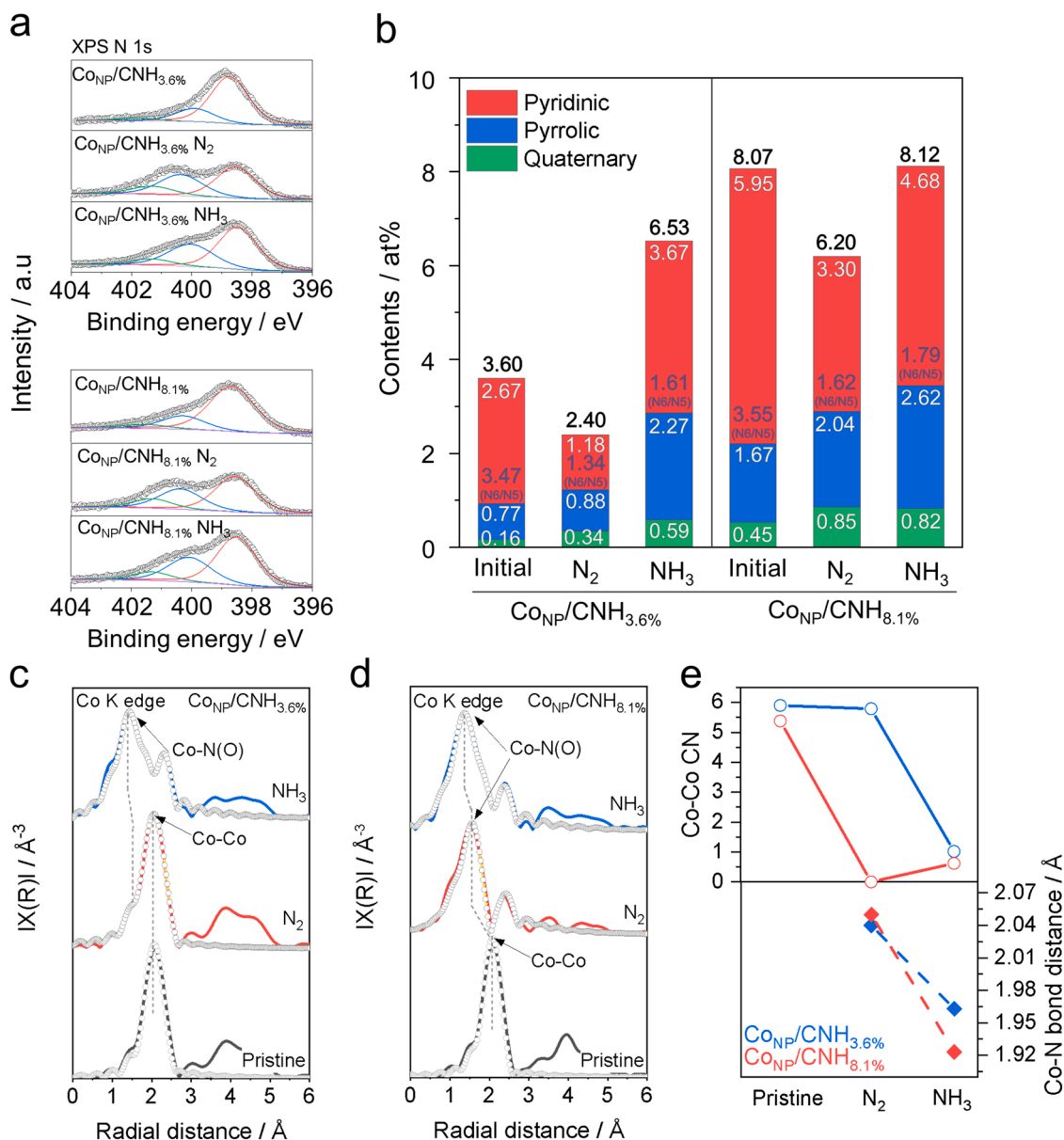


Fig. 2. (a) XPS N 1s spectra of CoNP/CNH_{3.6%} and CoNP/CNH_{8.1%} with N₂ and NH₃ treated samples. (b) The atomic contents of total nitrogen (top of columns, black color), pyridinic N (N6), pyrrolic N (N5), Quaternary N obtained from XPS N 1s results and ratio of N-6/N-5 (middle of columns, purple color) of CoNP/CNH_{3.6%} and CoNP/CNH_{8.1%} with N₂ and NH₃ treated samples. (c-d) FT-EXAFS curves (solid line) and fitting curves (circles) of CoNP/CNH_{3.6%} and CoNP/CNH_{8.1%} with N₂ and NH₃ treated samples. (e) Co-Co coordination number and Co-N bond distance obtained from EXAFS curve fitting of CoNP/CNH_{3.6%} and CoNP/CNH_{8.1%} with N₂ and NH₃ treated samples.

nitrogen species. It is considered that in CoNP/CNH_{3.6%} N₂, the total amount of nitrogen functional groups is insufficient to capture and stabilize the emitted Co atoms, leaving Co-NPs un-atomized. However, CoNP/CNH_{8.1%} N₂ has large amount of nitrogen functional groups enough for the atomization process of existing Co-NPs, which make it possible to produce a completely atomized SACs. It is also worth noting that the ratios of N-6 to N-5 (denoted as the N-6/N-5 ratio) for both CoNP/CNH_{3.6%} and CoNP/CNH_{8.1%} are 3.47 and 3.55, indicating that the N-6 species is dominant as a terminating group during nanocarbon synthesis from the bottom-up assembly process. Interestingly, the amounts of N-6 decreases, while that of N-5 increases, resulting in lower N-6/N-5 ratios of 1.34 for CoNP/CNH_{3.6%} N₂ and 1.62 for CoNP/CNH_{8.1%} N₂. It could be attributed to a restructuring process of preformed nitrogen functional groups by thermal transformation of N-6 into N-5 groups [35,36]. In the previous literature, the central metal atom coordinated with two N-5 and two N-6 sites at the defect of graphene was

known as the most stable and favorable configuration [28]. We can summarize the thermal transformation of Co-NPs into Co atoms under inert conditions, which is accompanied by utilizing the preformed nitrogen anchoring sites for capturing single metal atoms and inevitably involving favorable atomic reorganization of nitrogen functional groups toward M-N_x-C formation.

After the samples are annealed with ammonia, it is expected that there should be an additional effect of nitrogen doping on both graphitic carbon lattice and atomization process. The ammonia-treated CoNP/CNH_{3.6%} NH₃ show increased N doping levels of 6.53 at% than pristine catalysts with an N-6/N-5 value of 1.61, which is quite similar value to those of CoNP/CNH_{8.1%} N₂. Owing to the additional doping effect during the ammonia treatment, AMT process could be facilitated and well dispersed SACs could be obtained. In case of CoNP/CNH_{8.1%} NH₃, the nitrogen content was found to be almost same (8.12 at%) with the pristine catalyst. It is likely that there is maximum level of nitrogen

doping maintaining the crystalline structure of nanocarbon through ammonia treatment, since longer or high temperature condition start to damage the structure resulting in a loss of specific surface area [31].

Based on the XPS analysis, it has been demonstrated that the amount of nitrogen functional groups is indispensable for stabilizing metal atoms and dominate the degree of atomization process. Moreover, the N-6/N-5 ratios for both $\text{Co}_{\text{NP}}/\text{CNH}_{3.6\%} \text{NH}_3$ and $\text{Co}_{\text{NP}}/\text{CNH}_{8.1\%} \text{NH}_3$ are also rearranged to 1.61 and 1.79, respectively, which are quite similar values to those of N_2 annealing. This is also assumed that nitrogen functional groups were atomically restructured into a more favorable combination of N-6 and N-5 for both N_2 and NH_3 conditions, as AMT phenomena proceeds. It should be noted that the coupling additional nitrogen doping effect with favorable atomic restructuring of nitrogen sites can modify the defect sites and local structure of carbon network around M- N_x -C sites, possibly modulating local coordination structure near cobalt atoms. The detailed quantitative analysis for coordination structure can be further discussed through the EXAFS analysis.

3.3. Influence of annealing atmosphere on the local geometry of M- N_x -C sites

The local environments and properties of nitrogen anchoring sites can affect the coordination geometries of Co- N_x -C sites. To investigate the coordination structure of Co, we performed extended X-ray absorption fine structure (EXAFS) analysis. The detailed coordination structures were estimated from EXAFS curve fitting (Figs. S6-S7). The fitting parameters are listed in Table S2. In the Co K-edge EXAFS spectra (Fig. 2c-e), $\text{Co}_{\text{NP}}/\text{CNH}_{3.6\%}$ and $\text{Co}_{\text{NP}}/\text{CNH}_{8.1\%}$ show a prominent peak near 2 Å, which is assigned to Co-Co scattering in the Co crystals. The Co-Co coordination numbers in $\text{Co}_{\text{NP}}/\text{CNH}_{3.6\%}$ and $\text{Co}_{\text{NP}}/\text{CNH}_{8.1\%}$ are 5.90 and 5.38, respectively, indicating the presence of nanosized Co-NPs, whereas the coordination number of the Co foil is 12. A larger shoulder peak near 1.5 Å is observed in $\text{Co}_{\text{NP}}/\text{CNH}_{3.6\%} \text{N}_2$, which is the newly introduced Co-N bond. The Co-Co and Co-N coordination numbers of $\text{Co}_{\text{NP}}/\text{CNH}_{3.6\%} \text{N}_2$ are 5.79 and 2.42, respectively, suggesting that AMT partially proceeds during nitrogen annealing, while some of the Co-NPs remain. The lower Co-N coordination number (2.42) of the unsaturated feature could be due to insufficient nitrogen anchoring sites for the complete AMT process. However, the Co-Co bonds completely vanish, and the Co-N coordination number is 4.01 in $\text{Co}_{\text{NP}}/\text{CNH}_{8.1\%} \text{N}_2$, which indicates that the AMT process can be completed due to sufficient nitrogen anchoring sites. The fitting results reveal that the Co-N interatomic distances for both $\text{Co}_{\text{NP}}/\text{CNH}_{3.6\%} \text{N}_2$ and $\text{Co}_{\text{NP}}/\text{CNH}_{8.1\%} \text{N}_2$ are 2.04 Å and 2.05 Å, respectively, which are slightly longer than that of the ideal Co- N_4 structure (~1.85 Å for pyridinic-type Co- N_4 , ~1.94 Å for pyrrolic-type Co- N_4) [37,38]. It should be noted that the carbon structure with preformed nitrogen sites has loose crystalline structure, involving tensile strains and Stone-Wales like defects on carbon lattice, resulting in distorted Co- N_4 -C sites that are different from the ideal structure. As expected in the case of ammonia annealing, both $\text{Co}_{\text{NP}}/\text{CNH}_{3.6\%} \text{NH}_3$ and $\text{Co}_{\text{NP}}/\text{CNH}_{8.1\%} \text{NH}_3$ show EXAFS features of fully atomized Co- N_4 -C sites (Fig. 2c-e). Curiously, the interatomic distances of Co-N for $\text{Co}_{\text{NP}}/\text{CNH}_{3.6\%} \text{NH}_3$ and $\text{Co}_{\text{NP}}/\text{CNH}_{8.1\%} \text{NH}_3$ are 1.96 Å and 1.92 Å, respectively, which are shorter than those of their N_2 annealed counterparts. This confirms the important role of the ammonia annealing process, which promotes a restructuring of the carbon lattice around the nitrogen sites, forming improved Co- N_4 -C sites with less defective structures. A few Co-Co scatterings are considered for optimizing EXAFS fitting for both $\text{Co}_{\text{NP}}/\text{CNH}_{3.6\%} \text{NH}_3$ and $\text{Co}_{\text{NP}}/\text{CNH}_{8.1\%} \text{NH}_3$, and their coordination numbers are 1.02 and 0.62. There might be a small number of Co nanoclusters with a very small Co-Co coordination number less than 1, but most cobalt species are expected to be located predominantly as atomic Co- N_4 -C sites.

3.4. In situ characterization of the atomization mechanism from metal nanoparticles to a single metal atom

In situ TEM analysis can provide direct observation of atomic level transition phenomena and a better understanding of the conversion mechanism from Co-NPs to a single cobalt atom through real-time imaging of the dynamic AMT process. In the temperature window from room temperature (RT) to 900 °C under vacuum, the evolution of AMT in $\text{Co}_{\text{NP}}/\text{CNH}_{8.1\%}$ was recorded. The TEM images and particle numbers in the movie captured at different temperatures and times are shown in Fig. 3a-b. As the temperature increases to 800 °C, the Co-NPs move or disappear, and new metal particles are observed, indicating that atomization and reaggregation coexist. At 800 °C, atomization begins to suppress aggregation (5 % of particles disappeared). As demonstrated by Wei et al., thermal energy under high temperature overcomes the kinetic barrier of atomization, making the atomization process dominant.²⁴ After 240 s at 800 °C, 28 % of the Co-NPs disappear. When the temperature reaches 900 °C, the Co-NPs rapidly fade away, and after an additional four minutes, most of the nanoparticles vanish (93 % of the particles disappear). This observation provides direct evidence demonstrating that atomization-aggregation processes are competitive during the conversion of nanoparticles to single atoms. Energy dispersive X-ray spectroscopy elemental mapping shows that cobalt species are distributed in the carbon structure and are not evaporated. Since in situ TEM analysis under an ammonia atmosphere at high temperature is extremely challenging, we performed ex situ STEM analysis on ammonia-treated samples prepared at different temperature conditions (Fig. 3c). Co-NPs can be clearly seen as bright dots in both as-synthesized samples. The initially supported Co-NPs start to split into nanoclusters with loose crystalline structures and spread out the surrounding carbon network with atomized cobalt species at 400 °C. As the temperature increases, the fragmented cobalt nanoclusters gradually disappear, and the entire cobalt species are atomically fixed on the carbon structure.

The atomization mechanism from nanoparticles to single atoms was further investigated by an in situ temperature-resolved XAFS technique. Temperature-resolved X-ray absorption near edge spectroscopy (XANES) was applied at different temperatures (Fig. 3d). The labeled (1), (2), and (3) peaks associated with the typical electronic transition features for the Co foil can be seen in $\text{Co}_{\text{NP}}/\text{CNH}_{8.1\%}$, indicating the presence of cobalt crystals. As the temperature increases, noticeable features (1) and (2) gradually weaken and merge, and feature (3) disappears completely, indicating that the contribution of metallic nanoparticles significantly reduced by thermal annealing [39]. Interestingly, the intensity of the pre-edge feature (ca. 7715 eV) becomes stronger as the temperature increases, which is a shakedown satellite involving a 1 s to 4p_z transition related to ligand-to-metal charge transfer (Fig. S8) [31]. All these changes support the idea that the coordination structure around the Co atom changes during the annealing process. In situ EXAFS results provide further evidence for understanding the AMT process by revealing the changes in coordination environments (Fig. 3e). As the temperature increases, the marked (1) Co-Co scattering becomes shorter, confirming the conversion from Co-NPs to Co single atoms. Specifically, it should be noted that the intensities for Co-Co scattering gradually decrease as the temperature increases to 500 °C, which is considered to be the nanoclustering of Co-NPs with a loose crystalline structure. Then, the peak position becomes shorter as time passes at 500 °C, strongly indicating the initiation of atomization by forming atomic Co- N_4 -C sites. When a higher temperature state is reached at 700 °C, the peak position becomes much shorter due to the accelerated atomization rate. The combined in situ TEM and XAFS analysis provides direct evidence of AMT phenomena and confirms the sequential process of thermal decomposition of cobalt nanoclusters drifting through the carbon structure, and the emitted metal atoms are stabilized at nitrogen anchoring sites.

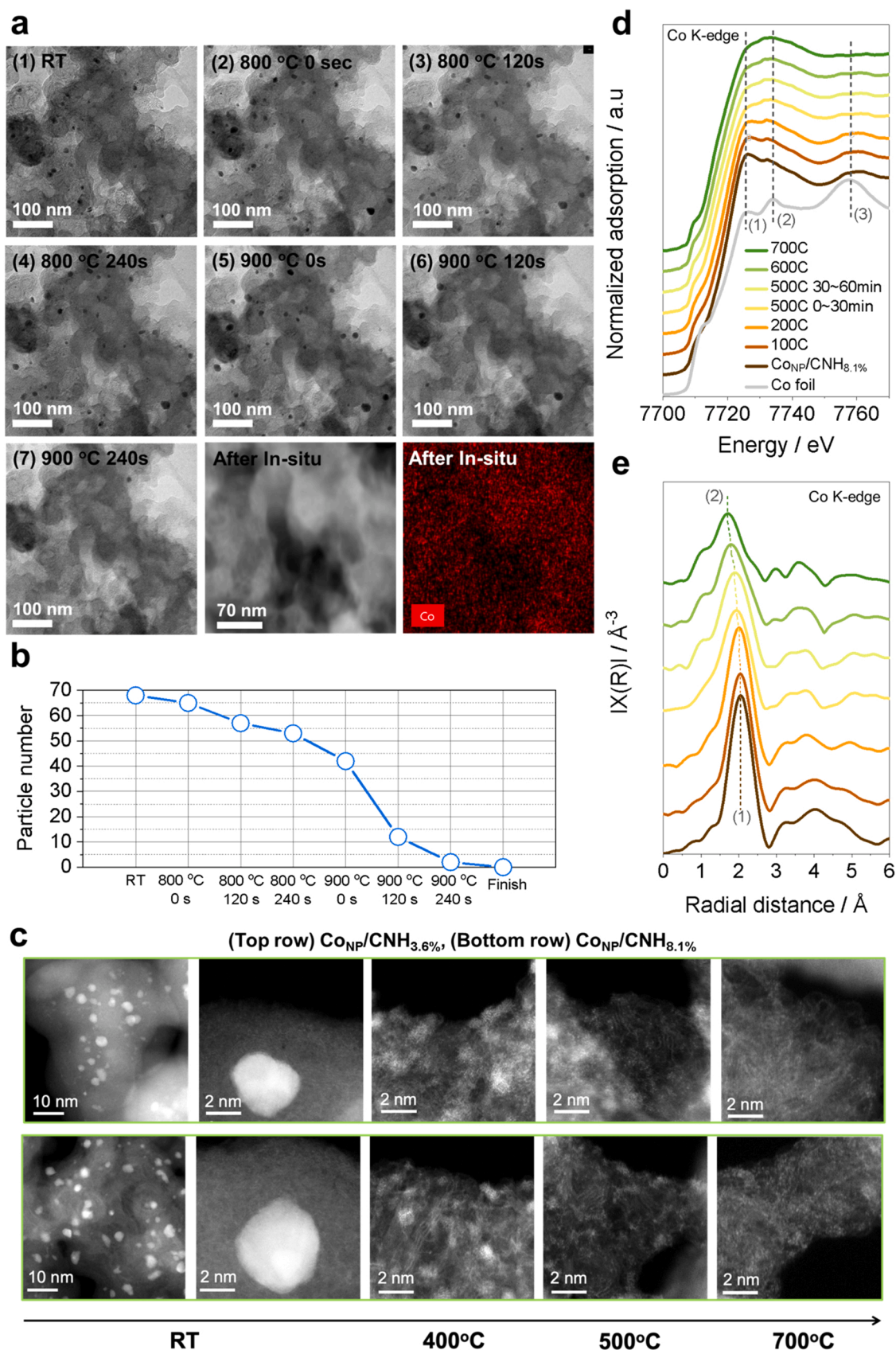


Fig. 3. (a) In-situ TEM image snapshots at various temperatures and times of $\text{Co}_{\text{NP}}/\text{CNH}_{8.1\%}$ under in-situ TEM analysis. (b) The number of particles at various temperatures and times. (c) HAADF-STEM images of (top) $\text{Co}_{\text{NP}}/\text{CNH}_{3.6\%}$, (bottom) $\text{Co}_{\text{NP}}/\text{CNH}_{8.1\%}$ as function of temperature under NH_3 . (d-e) In-situ temperature-dependent Co K-edge XANES and EXAFS curves at various temperatures and times under N_2 atmosphere.

3.5. Performance evaluation of oxygen reduction reaction and AEMFC tests

The ORR activities of all the catalysts were measured using linear sweep voltammetry (LSV) in a half-cell three-electrode system in oxygen-saturated 0.1 M KOH electrolyte (Fig. 4a). The pristine Co_{NP}/CNH_{3.6%} and Co_{NP}/CNH_{8.1%} exhibit very low half-wave potentials of 0.694 V_{RHE} and 0.710 V_{RHE}, respectively. However, the nitrogen-treated SACs exhibit higher half-wave potentials (0.777 V_{RHE} for Co_{NP}/CNH_{3.6%} N₂ and 0.803 V_{RHE} for Co_{NP}/CNH_{8.1%} N₂) than the pristine Co-NP

catalysts. The main contribution to the enhanced ORR performance is that large number of Co-N₄-C sites are driven by the atomization process, indicating that the catalytic performance is highly associated with the Co-N₄-C sites. Prior to comparing the ORR activity with ammonia annealing, we measured the LSV of Co_{NP}/CNH_{8.1%} NH₃ by changing the ammonia annealing temperature. The half-wave potential increases as the temperature for ammonia annealing increases because Co-NPs are gradually transformed into Co-N₄-C sites (Fig. S9). It should be noted that the half-wave potentials for both Co_{NP}/CNH_{3.6%} NH₃ and Co_{NP}/CNH_{8.1%} NH₃ are 0.824 V_{RHE} and 0.867 V_{RHE}, respectively, exhibiting

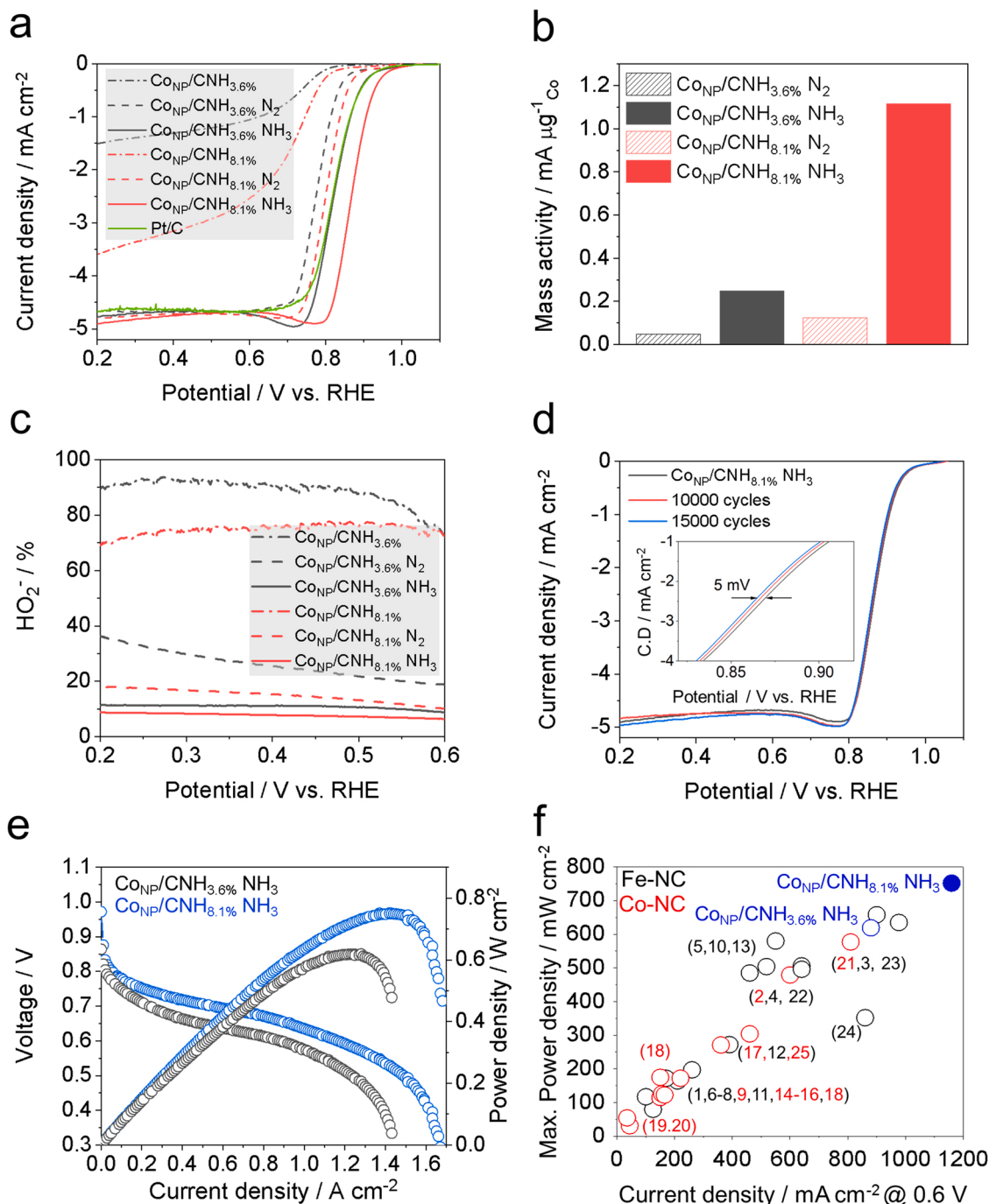


Fig. 4. (a) Polarization curves for the ORR activity of Co_{NP}/CNH_{3.6%} and Co_{NP}/CNH_{8.1%} with N₂ and NH₃ treated samples with commercial Pt/C catalysts. (b) Mass-normalized kinetic current density at 0.85 V vs RHE of Co_{NP}/CNH_{3.6%} and Co_{NP}/CNH_{8.1%} with N₂ and NH₃ treated samples. (c) HO₂⁻ selectivity determined using RRDE experiments measured in O₂-saturated 0.1 M KOH. (d) Polarization curves for the long-term durability of Co_{NP}/CNH_{8.1%} NH₃ under potential cycling and magnified graph (inset). (e) AEMFC performance of MEAs using Co_{NP}/CNH_{3.6%} NH₃, Co_{NP}/CNH_{8.1%} NH₃ as cathode electrode. (f) Comparison of the AEMFC single cell performance of recently reported M-NC catalysts (maximum power density and current density at 0.6 V).

much higher values than the nitrogen-treated samples. The half-wave potential of $\text{Co}_{\text{NP}}/\text{CNH}_{8.1\%} \text{ NH}_3$ is as much as 47 mV higher than that of a commercial platinum catalyst, indicating its superior intrinsic electrocatalytic activity. As shown in Fig. S10, the Tafel slopes of pristine $\text{Co}_{\text{NP}}/\text{CNH}_x\%$ were remarkably increased after thermal annealing, which is greatly attributed to the existing Co atoms and enhanced hierarchical porosity. Furthermore, the Tafel slopes for $\text{Co}_{\text{NP}}/\text{CNH}_x\% \text{ N}_2$ & $\text{Co}_{\text{NP}}/\text{CNH}_x\% \text{ NH}_3$ exhibits very close values to that of commercial Pt/C, indicating the similar ORR kinetic rate-determining step [31]. Analysis of the kinetic current density normalized by the mass loading of Co species would provide a more quantitative comparison of their intrinsic catalytic activities (Fig. 4b). The measured mass-normalized kinetic activity of $\text{Co}_{\text{NP}}/\text{CNH}_{3.6\%} \text{ NH}_3$ ($0.249 \text{ mA } \mu\text{g}_{\text{Co}}^{-1}$ at $0.85 \text{ V}_{\text{RHE}}$) is 5.08-fold higher than that of $\text{Co}_{\text{NP}}/\text{CNH}_{3.6\%} \text{ N}_2$ ($0.049 \text{ mA } \mu\text{g}_{\text{Co}}^{-1}$ at $0.85 \text{ V}_{\text{RHE}}$), providing clear evidence that the intrinsic activity of atomic Co- N_4 -C sites is higher than that of Co-NPs. It should be noted that the activity of $\text{Co}_{\text{NP}}/\text{CNH}_{8.1\%} \text{ NH}_3$ ($1.117 \text{ mA } \mu\text{g}_{\text{Co}}^{-1}$ at $0.85 \text{ V}_{\text{RHE}}$) is 9.01-fold higher than that of $\text{Co}_{\text{NP}}/\text{CNH}_{8.1\%} \text{ N}_2$ ($0.124 \text{ mA } \mu\text{g}_{\text{Co}}^{-1}$ at $0.85 \text{ V}_{\text{RHE}}$), even though most Co species are atomic Co- N_4 -C sites in both samples, suggesting the critical effect of the local structure around atomic Co species on the catalytic activity. Interestingly, the mass-normalized kinetic activity increases in the order of $\text{Co}_{\text{NP}}/\text{CNH}_{8.1\%} \text{ N}_2 < \text{Co}_{\text{NP}}/\text{CNH}_{3.6\%} \text{ NH}_3 < \text{Co}_{\text{NP}}/\text{CNH}_{8.1\%} \text{ NH}_3$, demonstrating that the activity enhancement originates from improved Co- N_4 -C sites with lower strain. The coupling effect between additional nitrogen doping and rearrangement of nitrogen atoms on carbon lattice and the corresponding formation of improved Co- N_x -C sites are the major contributors to a notably promoted catalytic activity of ORR.

Rotating ring-disk electrode (RRDE) experiments were further performed to quantify the fraction of HO_2^- ions and to confirm the ORR pathway of the catalysts (Fig. 4c and Fig. S11). The as-synthesized $\text{Co}_{\text{NP}}/\text{CNH}_x\%$ catalysts showed a high fraction of HO_2^- synthesis and an undesired two-electron ORR pathway ($n_{\text{avg}} = 2.22$ for $\text{Co}_{\text{NP}}/\text{CNH}_{3.6\%}$ and $n_{\text{avg}} = 2.50$ for $\text{Co}_{\text{NP}}/\text{CNH}_{8.1\%}$) due to the weak interaction between adsorbed oxygen and Co-NPs [40]. The nitrogen-treated $\text{Co}_{\text{NP}}/\text{CNH}_x\% \text{ N}_2$ catalysts showed a reduced fraction of HO_2^- synthesis, indicating that the reaction pathway becomes closer to the four electron transfer ($n_{\text{avg}} = 3.49$ for $\text{Co}_{\text{NP}}/\text{CNH}_{3.6\%} \text{ N}_2$ and $n_{\text{avg}} = 3.71$ for $\text{Co}_{\text{NP}}/\text{CNH}_{8.1\%} \text{ N}_2$). This is probably due to the enhanced catalytic activity from the newly formed partially atomized Co sites. $\text{Co}_{\text{NP}}/\text{CNH}_{3.6\%} \text{ N}_2$ still exhibits a higher HO_2^- fraction and lower n value than $\text{Co}_{\text{NP}}/\text{CNH}_{8.1\%} \text{ N}_2$ due to the presence of less active Co-NPs. The fraction of HO_2^- is more reduced in both NH_3 -treated samples. In particular, $\text{Co}_{\text{NP}}/\text{CNH}_{8.1\%} \text{ NH}_3$ ($n_{\text{avg}} = 3.85$) showed lower HO_2^- synthesis and higher n value than $\text{Co}_{\text{NP}}/\text{CNH}_{3.6\%} \text{ NH}_3$ ($n_{\text{avg}} = 3.79$) due to the relatively low Co-Co coordination number and more improved Co- N_4 -C sites.

In electrochemical devices, long-term stability tests are an important factor for evaluating catalyst properties. As shown in Fig. S12, the current retention curve for $\text{Co}_{\text{NP}}/\text{CNH}_{8.1\%} \text{ NH}_3$ exhibits excellent long-term stability with 95 % current retention after 50,000 s, which is much higher value compared to the commercial Pt/C catalyst (~40 % current retention). We further performed the methanol-tolerance experiment to examine the methanol crossover effect. As shown in Fig. S13, the ratio of current density for $\text{Co}_{\text{NP}}/\text{CNH}_{8.1\%} \text{ NH}_3$ showed no noticeable change even in the injection of 1 M methanol, which is much higher methanol resistance compared to the commercial Pt/C catalyst. To evaluate the ORR stability of $\text{Co}_{\text{NP}}/\text{CNH}_{8.1\%} \text{ NH}_3$, accelerated potential cycling tests were performed for 15,000 cycles with a potential window between 0.6 and 1.0 V_{RHE} (Fig. 4d and inset). Notably, the results show a negligible decay in half-wave potential of 5 mV, which is attributed to the stable nature of high temperature-derived Co- N_4 -C sites.

Finally, the potential of $\text{Co}_{\text{NP}}/\text{CNH}_{3.6\%} \text{ NH}_3$ and $\text{Co}_{\text{NP}}/\text{CNH}_{8.1\%} \text{ NH}_3$ as cathode materials in alkaline electrolyte membrane fuel cells (AEMFCs) was evaluated in single-cell experiments (Fig. 4e). The $\text{Co}_{\text{NP}}/\text{CNH}_{3.6\%} \text{ NH}_3$ catalyst exhibits a very high current density of

880 mA cm^{-2} at 0.6 V and a maximum power density of 619 mW cm^{-2} , which is almost comparable to those of the state-of-art Fe-NC catalyst. It should be noted that this value was obtained even at the very low catalyst loading of 1 mg cm^{-2} , which is impressive considering that the optimal catalyst loading for the Co-N-C catalyst using highly crystalline CNHs is 6 mg cm^{-2} in membrane electrode assemblies (MEAs) [31]. Remarkably, $\text{Co}_{\text{NP}}/\text{CNH}_{8.1\%} \text{ NH}_3$ exhibits an unprecedentedly high maximum power density of 752 mW cm^{-2} and a very high current density of 1160 mA cm^{-2} (Fig. 4f and Table S3). The unusually high single-cell performance of the M-N-C catalyst in this work might be attributed to several advantageous aspects of $\text{Co}_{\text{NP}}/\text{CNH}_{8.1\%} \text{ NH}_3$: 1) the large loading amount of active single atom Co species (0.456 at%) stably formed from the AMT mechanism, which was not obtained in our previous methodology or in the previous literature using highly crystalline nanocarbons, 2) the high intrinsic catalytic activity of a single Co site with an improved local structure around Co- N_4 -C sites, and 3) the well-developed hierarchical porous structure of 3D CNH for the simple formation of triple phase boundaries.

4. Conclusions

In summary, we demonstrated for the first time that AMT phenomena occur in highly crystalline nanocarbons with high metal loading. Our bottom-up arc discharge method provides ideal porous nanocarbons containing Co-NPs with tunable nitrogen anchoring sites, revealing the role of nitrogen anchoring sites in the atomization process. Our results revealed that the AMT process is dependent on the number of N-6 and N-5 sites and is accelerated by introducing additional nitrogen anchoring sites with favorable configurations through ammonia annealing. Moreover, ammonia annealing plays an important role in forming improved Co- N_4 -C sites by healing topological carbon defects. The combined in situ TEM and XAFS analysis confirms that Co-NPs thermally decomposed to nanoclusters and spontaneously atomized by anchoring metal atoms at the nitrogen sites. Consequently, the number of improved Co- N_4 -C sites was doubled by flash bottom-up synthesis of hierarchical porous nanocarbon and subsequent top-down AMT process. The $\text{Co}_{\text{NP}}/\text{CNH}_{8.1\%} \text{ NH}_3$ catalyst exhibits a higher half-wave potential than commercial Pt/C, by as much as 47 mV, with superior potential cyclic stability. The high-loading improved Co- N_4 -C sites are the key factors for boosting the catalytic activity. In the AEMFC single-cell experiment, a maximum power density of 752 mW cm^{-2} is achieved, exceeding all the reported Co-SACs using commercially available ionomer. We believe our findings will provide an avenue for a practical application of SACs in AEMFCs.

CRedit authorship contribution statement

Jae Young Jung: Conceptualization, Methodology, Validation, Data curation, Writing – original draft, Writing – review & editing; **Haneul Jin:** Characterization; **Min Woo Kim:** Methodology, Characterization; **Sungjun Kim:** Characterization; **Jeong-Gil Kim:** Characterization; **Pil Kim:** Characterization; **Yung-Eun Sung:** AEMFC analysis; **Sung Jong Yoo:** Validation; Writing – original draft, Writing – review & editing; **Nam Dong Kim:** Project administration, Writing – review & editing, Conceptualization, Validation.

Declaration of Competing Interest

The authors declare that they have no known competing financial interests or personal relationships that could have appeared to influence the work reported in this paper.

Data availability

The authors do not have permission to share data.

Acknowledgements

This work was supported by Korea Institute of Science and Technology (KIST) Institutional Program and Open Research Program (ORP), and the grants from the National Research Foundation of Korea Government (NRF, 2018M1A2A2061975, 2019R1A5A8080326, 2020R1A2C201423513).

Appendix A. Supporting information

Supplementary data associated with this article can be found in the online version at [doi:10.1016/j.apcatb.2022.122172](https://doi.org/10.1016/j.apcatb.2022.122172).

References

- [1] C. Zhu, S. Fu, Q. Shi, D. Du, Y. Lin, Single-atom electrocatalysts, *Angew. Chem. Int. Ed.* 56 (2017) 13944–13960.
- [2] C. Zhu, Q. Shi, S. Feng, D. Du, Y. Lin, Single-atom catalysts for electrochemical water splitting, *ACS Energy Lett.* 3 (2018) 1713–1721.
- [3] Y. Zhang, L. Guo, L. Tao, Y. Lu, S. Wang, Defect-based single-atom electrocatalysts, *Small Methods* 3 (2019), 1800406.
- [4] H. Fei, J. Dong, Y. Feng, C.S. Allen, C. Wan, B. Voloskiy, M. Li, Z. Zhao, Y. Wang, H. Sun, P. An, W. Chen, Z. Guo, C. Lee, D. Chen, I. Shakir, M. Liu, T. Hu, Y. Li, A. I. Kirkland, X. Duan, Y. Huang, General synthesis and definitive structural identification of MN₄C₄ single-atom catalysts with tunable electrocatalytic activities, *Nat. Catal.* 1 (2018) 63–72.
- [5] J. Chen, H. Li, C. Fan, Q. Meng, Y. Tang, X. Qiu, G. Fu, T. Ma, Dual single-atomic Ni-N₄ and Fe-N₄ sites constructing janus hollow graphene for selective oxygen electrocatalysis, *Adv. Mater.* 32 (2020), 2003134.
- [6] X. Li, W. Bi, L. Zhang, S. Tao, W. Chu, Q. Zhang, Y. Luo, C. Wu, Y. Xie, Single-atom Pt as Co-catalyst for enhanced photocatalytic H₂ evolution, *Adv. Mater.* 28 (2016) 2427–2431.
- [7] J. Fan, M. Chen, Z. Zhao, Z. Zhang, S. Ye, S. Xu, H. Wang, H. Li, Bridging the gap between highly active oxygen reduction reaction catalysts and effective catalyst layers for proton exchange membrane fuel cells, *Nat. Energy* 6 (2021) 475–486.
- [8] X. Cui, W. Li, P. Ryabchuk, K. Junge, M. Beller, Bridging homogeneous and heterogeneous catalysis by heterogeneous single-metal-site catalysts, *Nat. Catal.* 1 (2018) 385–397.
- [9] Y. Li, N. Wang, H. Lei, X. Li, H. Zheng, H. Wang, W. Zhang, R. Cao, Bioinspired N₄-metallomacrocycles for electrocatalytic oxygen reduction reaction, *Coord. Chem. Rev.* 442 (2021), 213996.
- [10] C. Tang, B. Wang, H.F. Wang, Q. Zhang, Defect engineering toward atomic Co-Nx-C in hierarchical graphene for rechargeable flexible solid Zn-Air batteries, *Adv. Mater.* 29 (2017), 1703185.
- [11] S. Zaman, L. Huang, A.I. Douka, H. Yang, B. You, B.Y. Xia, Oxygen reduction electrocatalysts toward practical fuel cells: progress and perspectives, *Angew. Chem. Int. Ed.* 60 (2021) 17832–17852.
- [12] P. Yin, T. Yao, Y. Wu, L. Zheng, Y. Lin, W. Liu, H. Ju, J. Zhu, X. Hong, Z. Deng, G. Zhou, S. Wei, Y. Li, Single cobalt atoms with precise n-coordination as superior oxygen reduction reaction, *Catal., Angew. Chem. Int. Ed.* 55 (2016) 10800–10805.
- [13] C. Zhu, S. Fu, J. Song, Q. Shi, D. Su, M.H. Engelhard, X. Li, D. Xiao, D. Li, L. Estevez, D. Du, Y. Lin, Self-assembled Fe-N-doped carbon nanotube aerogels with single-atom catalyst feature as high-efficiency oxygen reduction electrocatalysts, *Small* 13 (2017), 1603407.
- [14] L. Zhao, Y. Zhang, L.-B. Huang, X.-Z. Liu, Q.-H. Zhang, C. He, Z.-Y. Wu, L.-J. Zhang, J. Wu, W. Yang, L. Gu, J.-S. Hu, L.-J. Wan, Cascade anchoring strategy for general mass production of high-loading single-atomic metal-nitrogen catalysts, *Nat. Commun.* 10 (2019) 1278.
- [15] H. Yan, H. Cheng, H. Yi, Y. Lin, T. Yao, C. Wang, J. Li, S. Wei, J. Lu, Single-atom Pd₁/graphene catalyst achieved by atomic layer deposition: remarkable performance in selective hydrogenation of 1,3-butadiene, *J. Am. Chem. Soc.* 137 (2015) 10484–10487.
- [16] Y. Tang, C. Asokan, M. Xu, G.W. Graham, X. Pan, P. Christopher, J. Li, P. Sautet, Rh single atoms on TiO₂ dynamically respond to reaction conditions by adapting their site, *Nat. Commun.* 10 (2019) 4488.
- [17] M.M. Kauppinen, M.M. Melander, K. Honkala, First-principles insight into CO hindered agglomeration of Rh and Pt single atoms on m-ZrO₂, *Catal. Sci. Technol.* 10 (2020) 5847–5855.
- [18] Y. Dai, P. Lu, Z. Cao, C.T. Campbell, Y. Xia, The physical chemistry and materials science behind sinter-resistant catalysts, *Chem. Soc. Rev.* 47 (2018) 4314–4331.
- [19] C.H. Choi, W.S. Choi, O. Kasian, A.K. Mechler, M.T. Sougrati, S. Brüller, K. Strickland, Q. Jia, S. Mukerjee, K.J.J. Mayrhofer, F. Jaouen, Unraveling the nature of sites active toward hydrogen peroxide reduction in Fe-N-C catalysts, *Angew. Chem. Int. Ed.* 56 (2017) 8809–8812.
- [20] P. Yin, B. You, Atom migration-trapping toward single-atom catalysts for energy electrocatalysis, *Mater. Today Energy* 19 (2021), 100586.
- [21] J. Jones, H. Xiong, T. DeLaRiva Andrew, J. Peterson Eric, H. Pham, R. Challa Sivakumar, G. Qi, S. Oh, H. Wiebenga Michelle, I. Pereira Hernández Xavier, Y. Wang, K. Datye Abhaya, Thermally stable single-atom platinum-on-ceria catalysts via atom trapping, *Science* 353 (2016) 150–154.
- [22] M. Moliner, J.E. Gabay, C.E. Kliewer, R.T. Carr, J. Guzman, G.L. Casty, P. Serna, A. Corma, Reversible transformation of Pt nanoparticles into single atoms inside high-silica chabazite zeolite, *J. Am. Chem. Soc.* 138 (2016) 15743–15750.
- [23] G. Spezzati, Y. Su, J.P. Hofmann, A.D. Benavidez, A.T. DeLaRiva, J. McCabe, A. K. Datye, E.J.M. Hensen, Atomically dispersed Pd–O species on CeO₂(111) as highly active sites for low-temperature CO oxidation, *ACS Catal.* 7 (2017) 6887–6891.
- [24] Y. Qu, B. Chen, Z. Li, X. Duan, L. Wang, Y. Lin, T. Yuan, F. Zhou, Y. Hu, Z. Yang, C. Zhao, J. Wang, C. Zhao, Y. Hu, G. Wu, Q. Zhang, Q. Xu, B. Liu, P. Gao, R. You, W. Huang, L. Zheng, L. Gu, Y. Wu, Y. Li, Thermal emitting strategy to synthesize atomically dispersed Pt metal sites from bulk Pt metal, *J. Am. Chem. Soc.* 141 (2019) 4505–4509.
- [25] C. Cai, S. Han, Q. Wang, M. Gu, Direct observation of yolk-shell transforming to gold single atoms and clusters with superior oxygen evolution reaction efficiency, *ACS Nano* 13 (2019) 8865–8871.
- [26] Y. Qu, Z. Li, W. Chen, Y. Lin, T. Yuan, Z. Yang, C. Zhao, J. Wang, C. Zhao, X. Wang, F. Zhou, Z. Zhuang, Y. Wu, Y. Li, Direct transformation of bulk copper into copper single sites via emitting and trapping of atoms, *Nat. Catal.* 1 (2018) 781–786.
- [27] Z. Yang, B. Chen, W. Chen, Y. Qu, F. Zhou, C. Zhao, Q. Xu, Q. Zhang, X. Duan, Y. Wu, Directly transforming copper (I) oxide bulk into isolated single-atom copper sites catalyst through gas-transport approach, *Nat. Commun.* 10 (2019) 3734.
- [28] S. Wei, A. Li, J.-C. Liu, Z. Li, W. Chen, Y. Gong, Q. Zhang, W.-C. Cheong, Y. Wang, L. Zheng, H. Xiao, C. Chen, D. Wang, Q. Peng, L. Gu, X. Han, J. Li, Y. Li, Direct observation of noble metal nanoparticles transforming to thermally stable single atoms, *Nat. Nanotechnol.* 13 (2018) 856–861.
- [29] Y. Liu, G. Zhu, A. Li, J. Pei, Y. Zheng, W. Chen, J. Ding, W. Wu, T. Wang, D. Wang, J. Mao, Transforming cobalt hydroxide nanowires into single atom site catalysts, *Nano Energy* 83 (2021), 105799.
- [30] H. Zhou, Y. Zhao, J. Xu, H. Sun, Z. Li, W. Liu, T. Yuan, W. Liu, X. Wang, W.-C. Cheong, Z. Wang, X. Wang, C. Zhao, Y. Yao, W. Wang, F. Zhou, M. Chen, B. Jin, R. Sun, J. Liu, X. Hong, T. Yao, S. Wei, J. Luo, Y. Wu, Recover the activity of sintered supported catalysts by nitrogen-doped carbon atomization, *Nat. Commun.* 11 (2020) 335.
- [31] J.Y. Jung, J.-H. Jang, J.-G. Kim, K.-S. Lee, H.-K. Lim, P. Kim, R.P.H. Chang, J.-W. Park, S.J. Yoo, N.D. Kim, Flash bottom-up arc synthesis of nanocarbons as a universal route for fabricating single-atom electrocatalysts, *Small Methods* 5 (2021), 2100239.
- [32] B. You, N. Jiang, M. Sheng, W.S. Drisdell, J. Yano, Y. Sun, Bimetal-organic framework self-adjusted synthesis of support-free nonprecious electrocatalysts for efficient oxygen reduction, *ACS Catal.* 5 (2015) 7068–7076.
- [33] J.Y. Jung, Y.L. Hong, J.-G. Kim, M.J. Kim, Y.-K. Kim, N.D. Kim, New insight of tailor-made graphene oxide for the formation of atomic Co-N sites toward hydrogen evolution reaction, *Appl. Surf. Sci.* 563 (2021), 150254.
- [34] S. Li, Z. Fan, Nitrogen-doped carbon mesh from pyrolysis of cotton in ammonia as binder-free electrodes of supercapacitors, *Microporous Mesoporous Mater.* 274 (2019) 313–317.
- [35] J.Y. Jung, S. Kim, J.-G. Kim, M.J. Kim, K.-S. Lee, Y.-E. Sung, P. Kim, S.J. Yoo, H.-K. Lim, N.D. Kim, Hierarchical porous single-wall carbon nanohorns with atomic-level designed single-atom Co sites toward oxygen reduction reaction, *Nano Energy* 97 (2022), 107206.
- [36] S.M. Unni, S. Ramadas, R. Illathvalappil, S.N. Bhanage, S. Kurungot, Surface-modified single wall carbon nanohorn as an effective electrocatalyst for platinum-free fuel cell cathodes, *J. Mater. Chem. A* 3 (2015) 4361–4367.
- [37] S. Haldar, S. Bhandary, H. Vovusha, B. Sanyal, Comparative study of electronic and magnetic properties of iron and cobalt phthalocyanine molecules physisorbed on two-dimensional MoS₂ and graphene, *Phys. Rev. B* 98 (2018), 085440.
- [38] Y. He, S. Hwang, D.A. Cullen, M.A. Uddin, L. Langhorst, B. Li, S. Karakalos, A. J. Kropf, E.C. Wegener, J. Sokolowski, M. Chen, D. Myers, D. Su, K.L. More, G. Wang, S. Litster, G. Wu, Highly active atomically dispersed CoN₄ fuel cell cathode catalysts derived from surfactant-assisted MOFs: carbon-shell confinement strategy, *Energy Environ. Sci.* 12 (2019) 250–260.
- [39] J. Zhu, L. Xia, R. Yu, R. Lu, J. Li, R. He, Y. Wu, W. Zhang, X. Hong, W. Chen, Y. Zhao, L. Zhou, L. Mai, Z. Wang, Ultrahigh stable methanol oxidation enabled by a high hydroxyl concentration on Pt clusters/MXene interfaces, *J. Am. Chem. Soc.* 144 (2022) 15529–15538.
- [40] J. Shen, L. Meng, Y. Liu, C. Chen, Y. Zhu, C. Li, Preparation of Co-N carbon nanosheet oxygen electrode catalyst by controlled crystallization of cobalt salt precursors for all-solid-state Al–air battery, *RSC Adv.* 8 (2018) 22193–22198.